RESEARCH ARTICLE SUMMARY

CILIA AND FLAGELLA

Asymmetric distribution and spatial switching of dynein activity generates ciliary motility

Jianfeng Lin and Daniela Nicastro*

INTRODUCTION: Motile cilia and flagella are highly conserved, hairlike appendages of eukaryotic cells that propel the movement of cells or fluids. They play important roles in the normal development and health of many species, including humans. Flagellar beating is driven by the coordinated activities of multiple dynein isoforms that must be spatially and temporally regulated. Although the prevailing "switch-point" hypothesis posits that flagellar motility results from periodic switching of spatially restricted, asymmetrical activation of dyneins, no direct evidence has been reported, and how the thousands of dyneins inside a flagellum work together to generate flagellar motility remains elusive.

RATIONALE: Here we rapidly froze swimming sea urchin sperm cells and used cryo–electron tomography (cryo-ET) to image their beating flagella. Subtomogram averaging and classification analyses allowed us to identify and visualize the different activity states of individual dyneins and their regulators in situ. These conformational states were then mapped to their locations along the sinusoidal wave of the beating flagellum, for example, in relation to principal bend, reverse bend, or straight regions between bends. The results allowed us to elucidate the distinct roles played by various dyneins and to propose a model for the mechanism that underlies ciliary and flagellar motility.

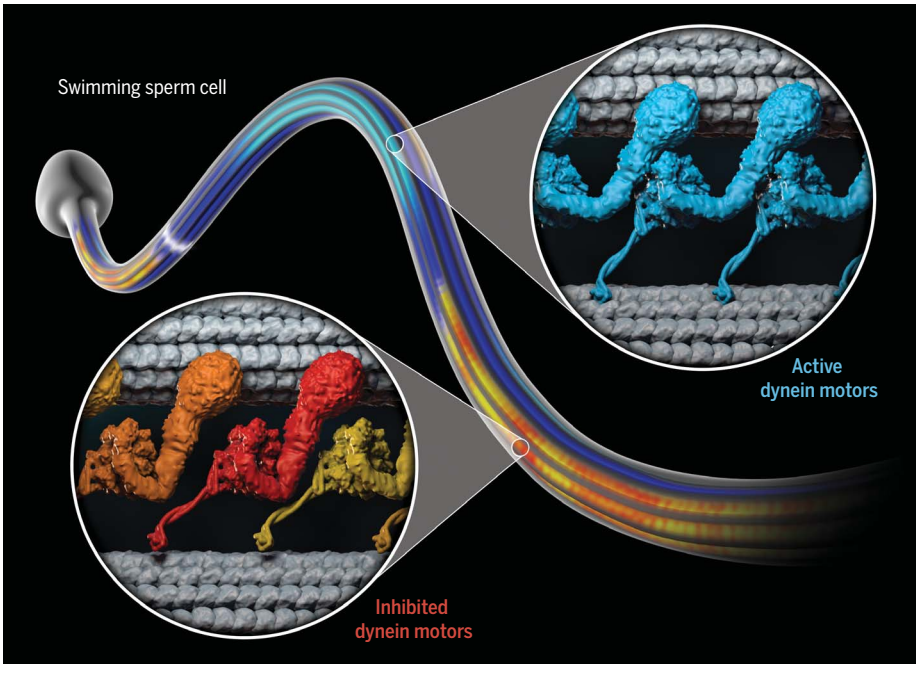

Asymmetric dynein activity underlies beating of cilia and flagella. Cryo-ET was used to image the active flagellum of swimming sea urchin sperm cells. Different activity states of the motility-driving dynein motors were identified. Magnified views show active (right) and inactive intermediate states (left). The distribution patterns of dynein conformations along the undulating waveform suggest a switch-inhibition mechanism for ciliary and flagellar motility.

RESULTS: The native three-dimensional structures of flagellar complexes were determined in situ with resolutions sufficient for identifying different activity states. Dyneins of immotile control flagella were found to be in post–power stroke conformations (unprimed, inactive states). By contrast, in beating flagella, most dyneins were in pre–power stroke conformations (primed, active states), with only a few dyneins in intermediate conformations. Moreover, for all outer dyneins, the intermediate and inactive conformations were only found in bent regions and were clustered on one side of the flagellum in a bend direction–dependent manner. For inner dyneins, certain isoforms (dyneins I1, a, d, and g) showed similar bend direction–dependent distribution patterns in bent regions of flagella, whereas the distribution patterns of other isoforms (dyneins b, c, and e) lacked obvious correlations with bending direction.

ON OUR WEBSITE

Read the full article at http://dx.doi.org/10.1126/science.aar1968

Our results revealed three key tenets that are important for generating flagellar motility: (i) The asymmetric distribution of dynein activity on opposite sides of the flagellum results in unidirectional bending, and (ii) the switching of dynein conformations between opposite sides causes the undulating waveform of beating flagella, both of which directly confirmed the switching aspect of the previously proposed switch-point hypothesis. (iii) In contrast to predictions, however, the findings also suggested the paradigm-shifting model that dyneins are active by default and that the asymmetry of dynein activity is driven by spatially restricted inhibition rather than activation of dyneins on alternating sides of the flagellum. This "switch-inhibition" mechanism was further supported by our analyses of a regulation-deficient *Chlamydomonas* mutant, which revealed that dyneins consumed adenosine triphosphate (ATP) and adopted pre–power stroke conformations, even though flagella were paralyzed.

CONCLUSION: Our comprehensive structural analysis combined with biochemical investigations provides an enhanced understanding of the distinct roles played by various dyneins and regulatory complexes in the motility of cilia and flagella and suggests critical modifications to previous hypotheses regarding robust molecular mechanisms underlying flagellar motility. Our study demonstrates that comparative cellular cryo-ET studies provide the conceptual framework and experimental tools to better understand molecular mechanisms and cellular functions. ■

The list of author affiliations is available in the full article online.
*Corresponding author. Email: daniela.nicastro@utsouthwestern.edu
Cite this article as J. Lin, D. Nicastro, *Science* **360**, eaar1968 (2018). DOI: 10.1126/science.aar1968

RESEARCH ARTICLE

CILIA AND FLAGELLA

Asymmetric distribution and spatial switching of dynein activity generates ciliary motility

Jianfeng Lin[1,2] and Daniela Nicastro[1,2]*

Motile cilia and flagella are essential, highly conserved organelles, and their motility is driven by the coordinated activities of multiple dynein isoforms. The prevailing "switch-point" hypothesis posits that dyneins are asymmetrically activated to drive flagellar bending. To test this model, we applied cryo–electron tomography to visualize activity states of individual dyneins relative to their locations along beating flagella of sea urchin sperm cells. As predicted, bending was generated by the asymmetric distribution of dynein activity on opposite sides of the flagellum. However, contrary to predictions, most dyneins were in their active state, and the smaller population of conformationally inactive dyneins switched flagellar sides relative to the bending direction. Thus, our data suggest a "switch-inhibition" mechanism in which force imbalance is generated by inhibiting, rather than activating, dyneins on alternating sides of the flagellum.

Motile cilia and flagella (*1*) are microtubule-based organelles that propel the movement of cells or fluids. They play essential roles in nearly all eukaryotes; for example, in humans, their motility is critical for embryonic development and organ function, and defects in ciliary assembly or motility lead to a range of diseases termed ciliopathies [reviewed in (*2*)]. From protozoa to humans, motile cilia share a highly conserved 9 + 2 axonemal structure, with nine doublet microtubules (DMTs, consisting of A- and B-tubules) surrounding a central pair complex (CPC) that contains two singlet microtubules with attached projections (Fig. 1A and fig. S1) [reviewed in (*3*)]. Along the DMT length, tens of thousands of dynein motors, regulators, and other axonemal complexes are spatially organized into 96-nm-long repeat units (Fig. 1, B and C, and fig. S1). Ciliary motility is driven by the coordinated activities of multiple dynein isoforms that must be spatially and temporally regulated (*4*, *5*).

Dyneins are multisubunit enzymes that hydrolyze adenosine triphosphate (ATP) to transport cargo toward the minus end of microtubules (*5*–*7*). Their major subunits are one to three large dynein heavy chains (HCs) and several smaller intermediate and light chains that associate with the N-terminal tail of the HC, assisting in oligomerization and cargo binding (Fig. 1D) (*5*). The motor unit of the dynein HC can be divided into four parts (Fig. 1D): the ATP-hydrolyzing head (a ring of six AAA+ domains), the linker (lever arm between head and tail), the coiled-coil stalk, and the microtubule-binding domain (MTBD) at the stalk's tip (*5*, *7*). Typically, cells encode a single dynein HC isoform for the homodimeric cytoplasmic dynein that fulfills different roles in a plethora of cellular processes, from retrograde transport to mitosis. By contrast, ciliary motility requires more than a dozen different axonemal dynein HC isoforms (*8*). Usually, each axonemal repeat contains 11 dynein complexes that attach permanently with their tails to the A-tubule and form two distinct rows of "arms" along the length of each DMT (Fig. 1C and fig. S1B). One row consists of heterodimeric (α- and β-HC; for example, in sea urchin and human) or heterotrimeric (for example, in protozoa) outer dynein arms (ODAs). In some species, the ODAs of one specialized DMT (usually DMT1 or DMT5) are replaced by nonmotile, cross-linking structures, such as the o-SUB5-6 bridge on DMT5 of sea urchin sperm flagella (Fig. 1A) (*9*). The second row consists of the inner dynein arms (IDAs), which include the heterodimeric (1α- and 1β-HC) I1 dynein and six dyneins (a to e, and g) that have a single HC each (Fig. 1C and fig. S1B). Thus, each repeat contains 16 or 20 dynein motor heads (fig. S1B). Previous in vitro biochemical studies have demonstrated markedly different molecular motor properties (e.g., velocity, processivity, regulatory function) for individual axonemal dyneins (*10*). However, how the various activities of these multiple dyneins are spatially and temporally coordinated to affect ciliary motility remains unknown.

To generate ciliary bending, the dyneins from DMT n walk toward the minus end of the neighboring DMT n + 1 in an ATP-dependent manner, causing sliding between these adjacent DMTs (fig. S2). In intact cilia, the extent of sliding is restricted by the basal body and interdoublet linkers (for example, the nexin link), converting the interdoublet sliding into axonemal bending in the direction of DMT n + 1 (fig. S2) (*11*, *12*). The undulatory motion of cilia and flagella requires bending in alternate directions. The prevailing "switch-point" hypothesis posits that, during ciliary beating, spatially restricted dynein activity switches regularly by means of alternate activation of dyneins on opposite sides of the axoneme (*13*). This model is supported by several lines of indirect evidence (*14*–*16*) derived from genetic (for example, phenotypes of motility mutants) and biochemical (for example, in vitro assays, DMT extrusion) approaches, as well as conventional electron microscopy with limited resolution and in silico simulations. However, to date, the activity states of individual dyneins in the context of intact beating cilia, and how these contribute to the mechanics of motility, have not been directly demonstrated. It is also largely unknown how the many dynein isoforms are coordinated and how switching of the bending direction is regulated.

To directly test the switch-point hypothesis and define the structural basis for the spatially and temporally coordinated activity of multiple dyneins during ciliary motility, we rapidly froze swimming sea urchin sperm cells and applied cryo–electron tomography (cryo-ET), subtomogram averaging, and particle classification to identify the activity state of individual dyneins. These activity states were then mapped to their locations in the axoneme and in relation to bent or straight regions along the beating flagellum, allowing a direct correlation between structure and function. Our higher-resolution structural analyses elucidate the distinct roles played by various dyneins and regulators to ensure their coordinated activity for robust ciliary beating.

Cryo-ET allows the visualization of the activity states of individual dynein motors along beating flagella

Swimming sea urchin sperm cells with actively beating flagella (active flagella; fig. S3 and movie S1) were rapidly frozen to trap the dynein motors and regulators in their current conformational states (*17*). The natively preserved flagella were then imaged by cryo-ET along their entire length except for the very base of the flagellum, because the ice close to the sperm head was too thick for electrons to penetrate under low-dose conditions. After calculating the three-dimensional (3D) reconstruction of the flagella (Fig. 1, E to G), subtomograms containing dyneins and regulators were extracted, aligned, and averaged (fig. S3 and table S1) (*18*). Then, structural classification (*19*) was performed to separate the different activity states of the dyneins into class averages on the basis of changes in the overall molecule shape and the relative position of major domains within and between molecules (Fig. 2, fig. S3, and table S2).

Dyneins generate force through an ATP-consuming cycle of pre– and post–power stroke conformational changes that cause relative motion

[1]Departments of Cell Biology and Biophysics, University of Texas Southwestern Medical Center, Dallas, TX 75390, USA.
[2]Department of Biology, Rosenstiel Basic Medical Sciences Research Center, Brandeis University, Waltham, MA 02454, USA.
*Corresponding author. Email: daniela.nicastro@utsouthwestern.edu

especially between dynein's linker and head domains, resulting in a power stroke that pulls the tail-bound DMT (cargo) toward the minus end of the neighboring DMT (track) [reviewed in (7)]. Extensive previous studies of isolated dynein have related dynein's mechanochemical and stepping cycle to changes in its structure (7), including the 3D atomic structures in different conformational states. This allowed us to interpret the activity state of the class-averaged dynein structures observed here with high confidence (Fig. 2, A to C′). We identified several distinct conformations for all axonemal dynein isoforms (table S2). For example, it has been shown that a small angle between the dynein linker and stalk domains is representative of dynein's "inactive" post–power stroke conformation (7) (Fig. 2, A, A′, F, and G). By contrast, a large angle is indicative of a "primed" ("spring-loaded") pre–power stroke conformation (7) (Fig. 2, B to C′, K, and L). In axonemes, we never observed the autoinhibited "phi particle" that was recently described for cytoplasmic dynein (20). The linker of the phi dimer is in a primed position, but the second HC is rotated 180°; thus, the stalk would point toward the microtubule plus end, which could likely not form between properly assembled axonemal dyneins because of geometric constraints. The previous structure-function studies allowed us to identify the activity state of individual dynein motors relative to their positions within the axoneme and along the beating flagellum.

Asymmetric and bend direction–dependent distribution of the activity of outer dyneins

To confirm our structure and function assignments, we first analyzed immotile flagella that were inactivated by using either the adenosine triphosphatase (ATPase) inhibitor erythro-9-(2-hydroxy-3-nonyl)adenine (EHNA) (immotile-inhibited; Fig. 1E, fig. S3A, and movie S2) or ATP-depleted, demembranated flagella (immotile-demembranated; Fig. 1F and fig. S3A). The

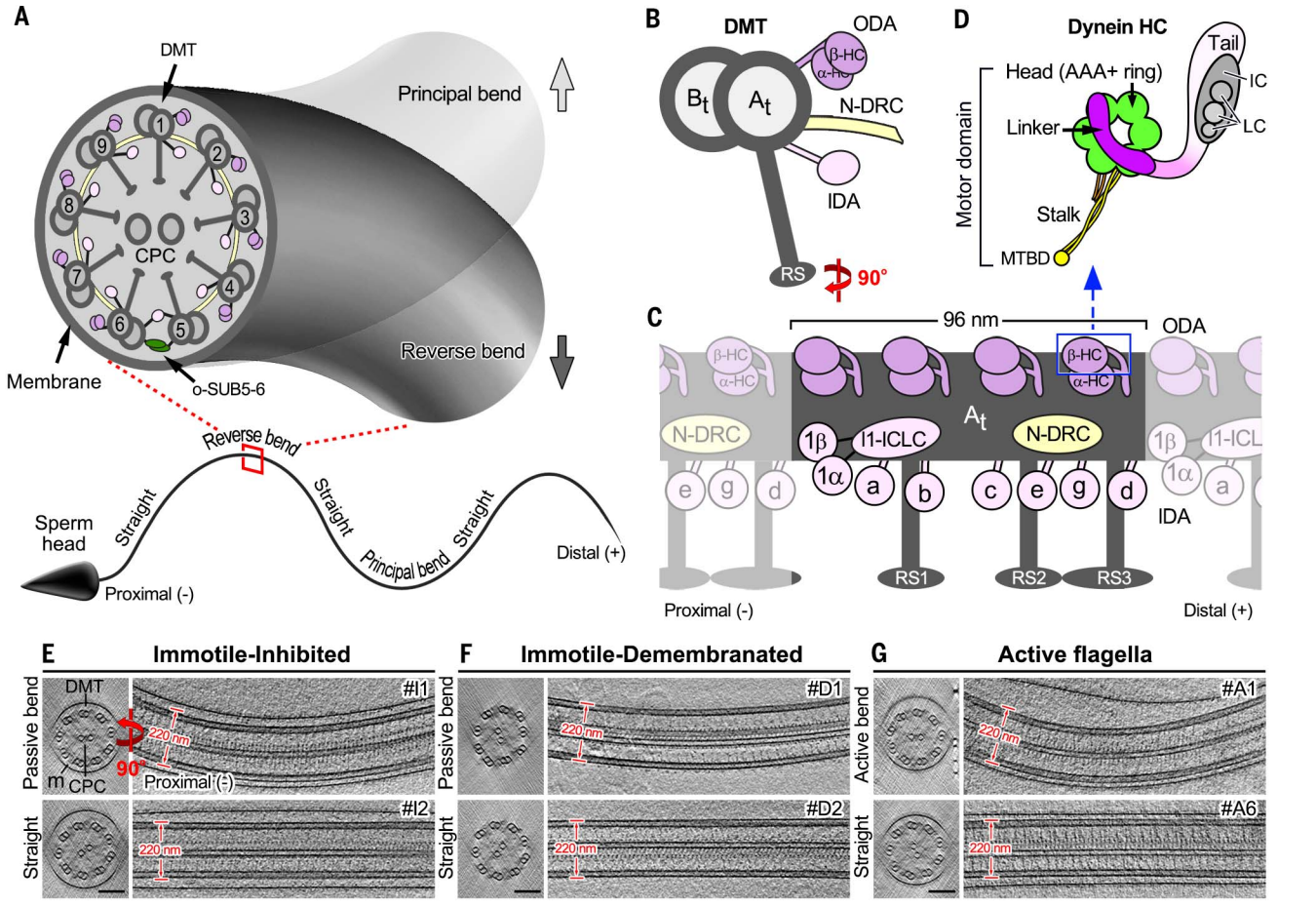

Fig. 1. 3D visualization of native sea urchin sperm flagella using cryo-ET. (**A**) Diagrams of a sea urchin sperm (bottom) and zoom-in of the flagellum (top). The flagellar bending directions toward DMT1 (principal bend) or the o-SUB5-6 bridge (reverse bend) are indicated (note that the nomenclature of bend direction in relation to DMT numbers is not consistent among species). The o-SUB5-6 bridges on DMT5 of sea urchin sperm flagella replace the ODAs. Microtubule polarity is indicated by "+" and "–" ends. (**B** and **C**) Cross-sectional (B) and longitudinal (C) views of a DMT, which consists of 96-nm-long repeat units. Each repeat contains four ODAs with two heavy chains (α- and β-HC), the I1 dynein with two HCs (1α and 1β) and an intermediate–light chain complex (I1-ICLC), and six single-headed inner dyneins (IDAs a to e, and g). A_t, A-tubule; B_t, B-tubule; RS, radial spoke. (**D**) Schematic of domain organization of a dynein HC [magnified view of region outlined in blue in (C)] with associated ICs and LCs that bind to the N-terminal tail domain of the HC and facilitate oligomerization as well as cargo binding (in cilia the cargo is the DMT A-tubule). (**E** to **G**) Tomographic slices of representative bent and straight regions from sea urchin sperm flagella in the following states, as viewed in cross sections and longitudinal sections: intact inhibited immotile flagella (E), demembranated immotile (ATP-free) axonemes (F), and intact active flagella (G). Even in the controls with an immotile flagella and/or axoneme, we occasionally observed bends [(E) and (F), top]. However, these are likely passive bends induced by outside forces (for example, liquid motion during sample preparation). m, membrane. Scale bar in (E) to (G) is 100 nm.

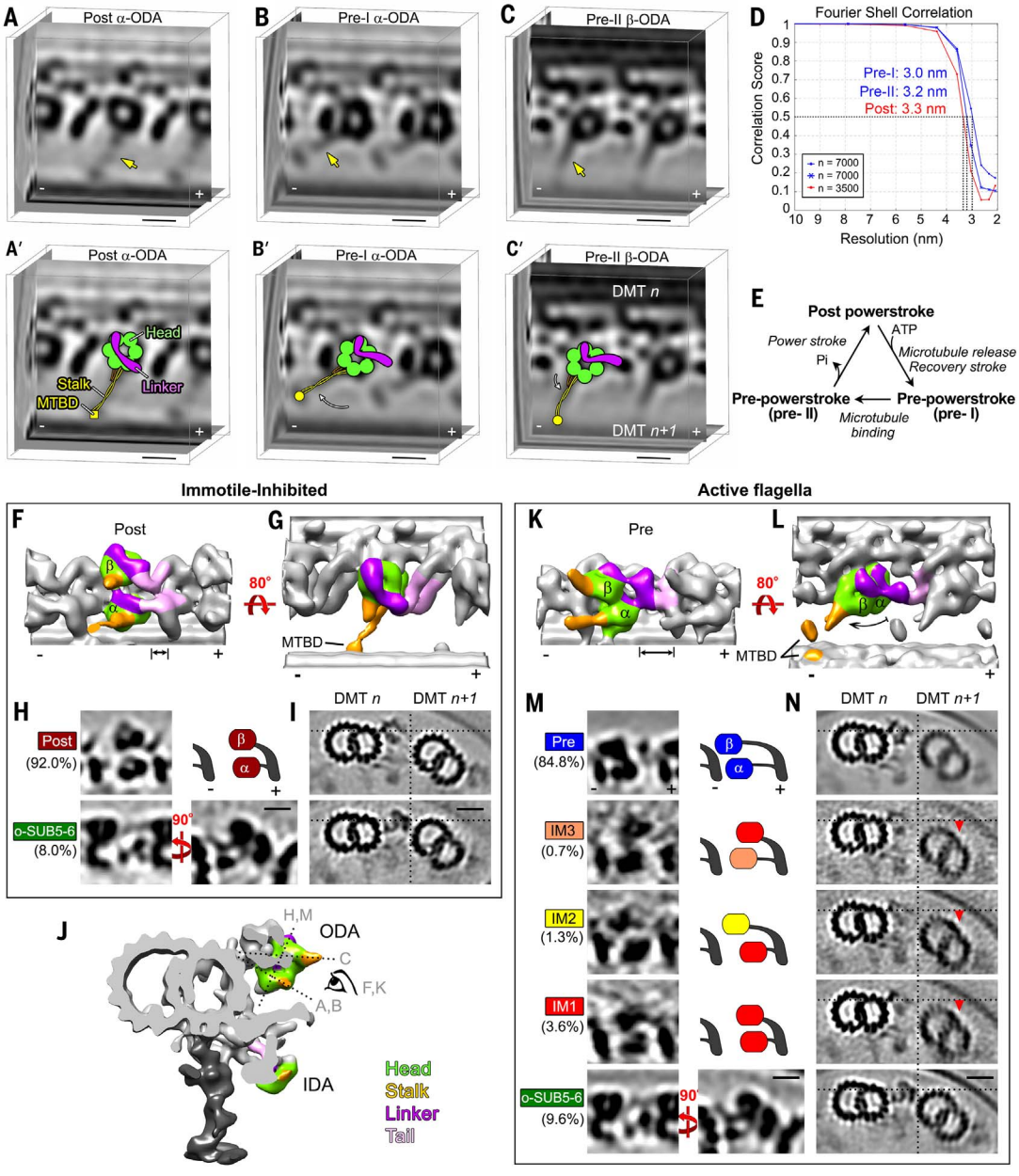

Fig. 2. The outer dyneins exhibit distinct conformations in active sea urchin sperm flagella. (**A** to **C′**) Tomographic slices of ODAs show the three predominant activity states without [(A) to (C)] and with [(A′) to (C′)] schematic model superimposed: the post–power stroke conformation (post) [(A) and (A′)] in immotile flagella and the pre–power stroke states pre-I [(B) and (B′)] and pre-II [(C) and (C′)] in active flagella. Note that the stalk (yellow arrow) with MTBD is microtubule bound in both the post (A) and the primed pre-II (C) states and detached in the primed pre-I state (B) (*17*). (**D**) Spatial resolution of the class averages shown in (A) to (C), as determined by Fourier shell correlation (FSC = 0.5). (**E**) Transitions between dynein conformations. Interpretation of the nucleotide states is based on (*51*). P_i, inorganic phosphate. (**F** and **G**) 3D isosurface renderings of the class average post conformation that has both dynein heads in the post–power stroke state. Domain coloring is as shown in the legend in (J). The double-headed arrow in (F) highlights the small gap between the dynein heads and tails. (**H** and **I**) Longitudinal [(H), left] and cross-sectional (I) tomographic slices of the two class averages (ODA-post and o-SUB5-6) in inhibited immotile flagella and a simplified diagram [(H), top right] of the two dynein head positions. The percentage of subtomograms included in each average is indicated. (**J**) 3D isosurface rendering of the averaged axonemal repeat of active flagella, as viewed in cross section. The location of the tomographic slices shown in (A) to (C), (H), and (M) and the viewing direction of (F) and (K) are indicated by their corresponding letters. (**K** and **L**) 3D isosurface renderings of the class average pre conformation that has both dynein heads in the pre–power stroke state. The double-headed arrow in (K) highlights the large gap between the dynein heads and tails. (**M** and **N**) Longitudinal [(M), left] and cross-sectional (N) tomographic slices and simplified diagrams [(M), right] show changes in the dynein-head position of the four averaged ODA classes (pre, IM3, IM2, and IM1) and o-SUB5-6 identified in active flagella. The dynein heads are color coded depending on their conformations. Dotted lines indicate the relative positions of neighboring DMTs, and red arrowheads highlight the positional shift of DMT *n* + 1 in intermediate states IM1 to IM3. Scale bars are 10 nm in (A) to (C′), (H), and (M) and 20 nm in (I) and (N).

occasionally observed bends in these immotile samples (Fig. 1, E and F) were most likely passive bends induced by external force (for example, liquid flow) during sample freezing. As expected for immotile flagella and axonemes, all outer dynein motors (ODA α- and β-HC) were in the tightly microtubule-bound, inactive post–power stroke conformation (Fig. 2, A, A′, and F to I, and fig. S4, post), regardless of whether the flagella were straight or passively bent (Fig. 3, A and B, and fig. S5).

The classification algorithm also automatically identified a class containing the o-SUB5-6 bridge structures on DMT5 of inhibited (and active) flagella (bottom rows in Fig. 2, H, I, M, and N). As previously reported, the o-SUB5-6 bridge structures cross-link DMT5 and DMT6 in sea urchin sperm flagella (*9*) and likely form a fairly rigid plane parallel to the two CPC microtubules that are also rigidly cross-linked by a specialized bridge structure (*21*). Together, these two complexes are thought to restrict the flagellar bending direction perpendicular to the planar arrangement of DMT5 and DMT6 and the CPC microtubules, respectively, to impede flagellar twisting or out-of-plane beating (*10*, *15*).

The switch-point hypothesis and prevailing view of flagellar motility predict that active and

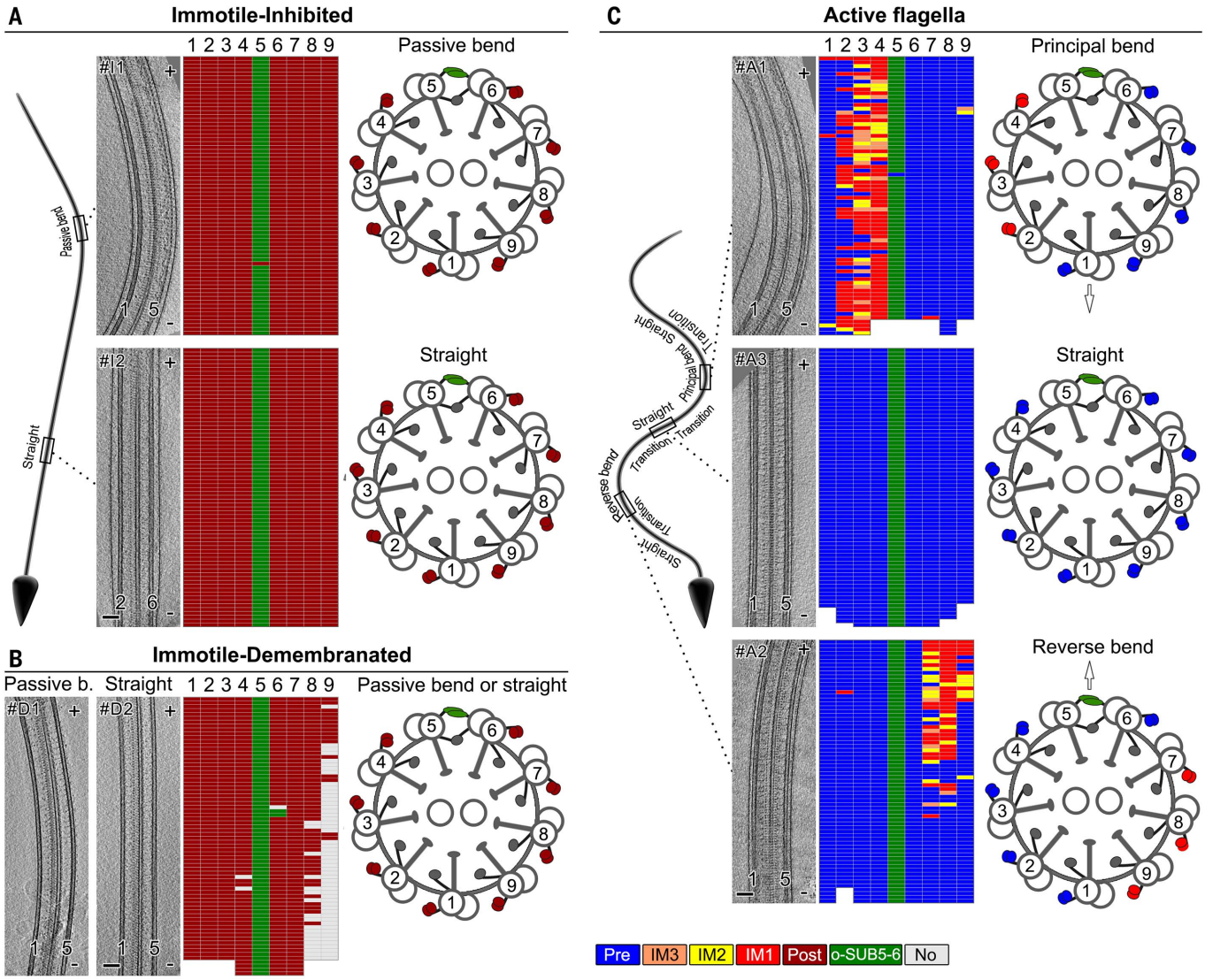

Fig. 3. The distinct conformations of outer dyneins in active sea urchin sperm flagella correlate with bend direction. (**A** to **C**) Distributions of ODA conformations in different regions of individual immotile-inhibited (A), immotile-demembranated (B), and active (C) flagella. For each flagellum, the following is shown: a longitudinal tomographic slice (left), the distribution pattern of ODA conformations (middle), and a diagram of an axonemal cross section (right) (arrows indicate bend directions). In the distribution patterns, the ODA repeats on the nine DMTs (1 to 9) are schematically shown as individual grids; the grid color represents the conformational state of each ODA repeat as shown in the legend. Diagrams of an actively swimming sperm cell (C) and an immotile-inhibited sperm cell (A) were depicted to indicate specific functional regions of the flagellum. Scale bars, 100 nm.

primed dynein states will be found spatially restricted to only a few DMTs on one side of curved regions of the flagellum (*13*). Surprisingly, however, the predominant class of outer dyneins throughout intact flagella had both motor domains in active pre–power stroke conformations (Fig. 2, B to C′ and K to N, pre; and movie S3), in which the dynein heads are closer to the minus end of the DMT relative to the post–power stroke conformation (Fig. 2, compare K with F) and the linkers are in the primed position (Fig. 2, compare L with G). In addition, α- and β-ODA are in the microtubule-detached pre-I and the microtubule-bound pre-II states, respectively (Fig. 2, B to C′).

The remaining three outer dynein classes in active flagella showed intermediate (IM) conformations (IM1 to IM3) that were either post–power stroke–like (Fig. 2M, IM1) or had the dynein head located somewhere between the post– and the pre–power stroke positions (Fig. 2M, IM2 and IM3). In the averages of intermediate conformations, the stalk density was blurred out and thus not clearly visible. This is typically observed when structures that exhibit positional heterogeneity are averaged and suggests that the stalks and MTBDs in these intermediate states were detached from or only weakly bound to the DMT, rather than tightly bound to the DMT. On the basis of the observed structural features, it is likely that the intermediate conformations (IM1 to IM3) of the outer dyneins neither generate force nor resist interdoublet sliding.

Intriguingly, the intermediate conformations were spatially restricted to one side of only bent regions of active flagella. Specifically, depending on the bend direction, they were found either on DMTs 2 to 4 in principal bend regions, or on DMTs 7 to 9 in reverse bends (Fig. 3C). Our direct visualization of the spatial organization of dynein conformation supports two key predictions of the switch-point hypothesis (*13*): (i) Active and inactive states of the outer dyneins are indeed asymmetrically distributed on opposite sides of beating flagella, allowing the actively walking dyneins to drive unidirectional bending, and (ii) to alternate the bending direction during beating, the sides on which the outer dyneins generate force switch. However, in contrast to previous

predictions, in straight regions of active flagella, all outer dyneins were uniformly in primed pre–power stroke conformations (Fig. 3C). Even in bent regions of the flagella, the outer dyneins adopted their pre–power stroke states on at least five of the eight DMTs with ODAs. By contrast, the population of conformationally inactive dyneins was spatially restricted to two to three DMTs and switched flagellar sides relative to the bending direction (Fig. 3C). These data strongly suggest that, at steady state, most outer dyneins readily bind ATP—which is omnipresent in the ciliary matrix—and adopt active, pre–power stroke states within their mechanochemical cycle. This interpretation is consistent with previous in vitro results, including (i) that most isolated dyneins can undergo mechanochemical cycles upon addition of just ATP and Mg^{2+} (*22*) and (ii) that ATP-deprived axonemes that have been treated with protease to cleave interdoublet linkers require only the addition of ATP to extrude DMT and undergo axoneme disintegration through linear interdoublet sliding (*12*, *23*). Thus, when the outer dyneins on all DMTs are in their active states, the flagellum is straight, that is, the forces generated on opposite sides of the flagellum are balanced and no net bending force is generated. Spatially clustered inactive dyneins disrupt this balance, allowing dyneins on the opposite side of the flagellum to drive motility.

Inner dynein isoforms also show asymmetric and bend direction–dependent distribution of activity

Similar to the results for outer dyneins, inner dyneins were predominantly in the inactive post–power stroke state in immotile controls (Figs. 4B and 5A and fig. S5; post) and in the primed pre–power stroke conformations in active flagella (Figs. 4, B and C, and 5, B and G, pre; and movie S4). In addition, for four of the inner dynein isoforms—dyneins a, g, d (Fig. 4C), and I1 dynein (Fig. 5G)—the distribution of the smaller population of intermediate conformations (IM1 and IM2) was highly correlated with the bend direction, that is, they were found either on DMTs 1 to 4 in principal bend regions or on DMTs 6 to 9 in reverse bends of active flagella. This suggests that these inner dyneins contribute to flagellar motility through the same conformational switching mechanisms as seen for the outer dyneins.

In contrast to the outer dyneins, however, we found overall more conformational heterogeneity and specializations among the inner dynein

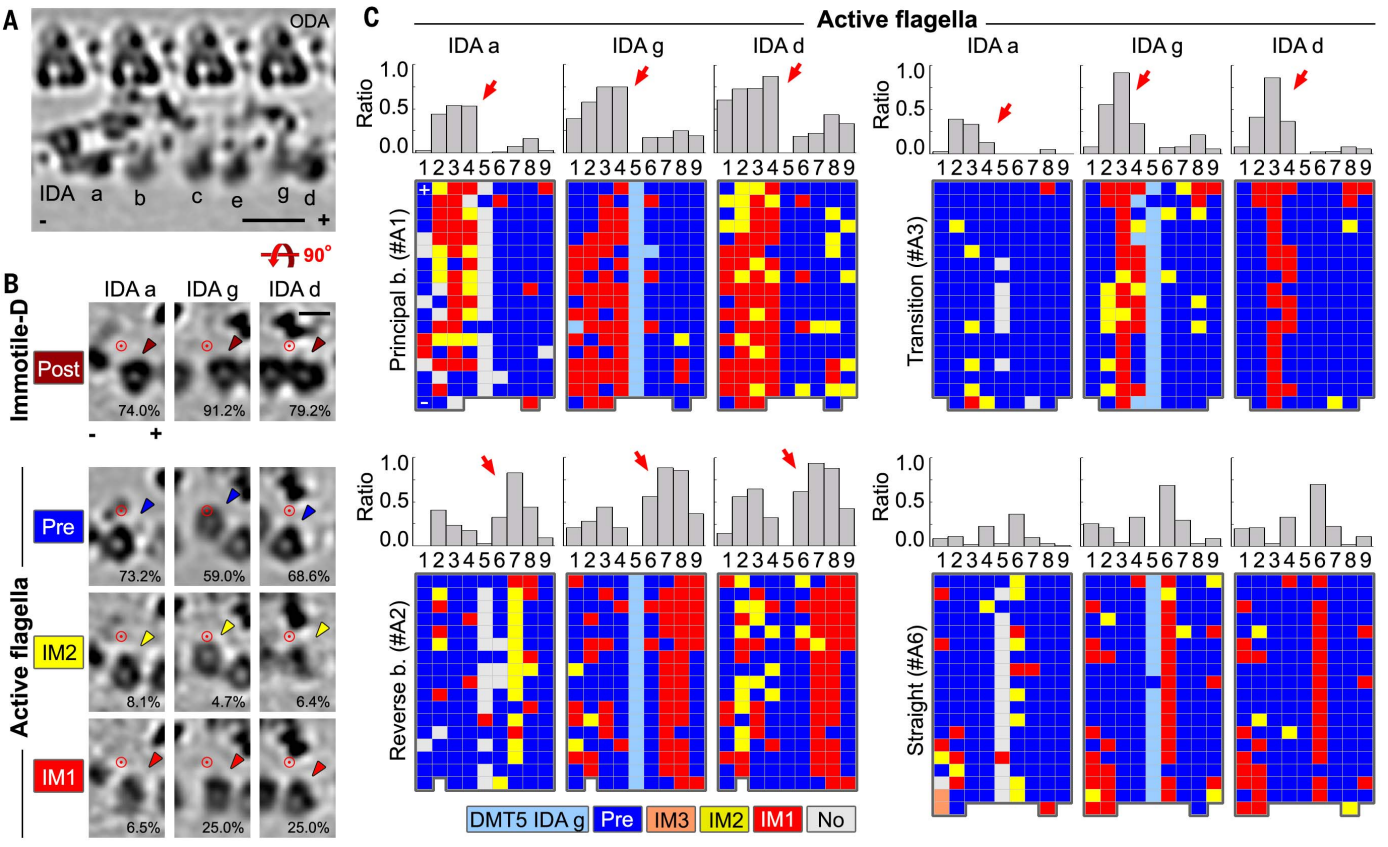

Fig. 4. The inner dyneins a, g, and d exhibit distinct conformations that correlate with bend direction in active sea urchin sperm flagella. (**A**) A longitudinal tomographic slice of the averaged 96-nm repeat of active flagella shows the arrangement of IDAs a to e, and g. (**B**) Tomographic slices of class averages of IDAs a, g, and d in immotile-demembranated axonemes (immotile-D) and active flagella. The percentage of subtomograms included in each class average is indicated. The identified inner dynein conformations are post–power stroke (post, dark red), pre–power stroke (pre, blue), and the intermediates IM2 (yellow) and IM1 (red). Arrowheads point at the particular dynein heads. The red circles mark identical locations in each column to allow better correlation of positional changes of the IDA heads. (**C**) Distributions of the activity states of IDAs a, g, and d in four functional regions of the flagellar wave of active flagella. For each inner dynein isoform, an averaged histogram (top) and color-coded distribution pattern (bottom) of a representative flagellum are shown. The histograms depict the ratios of intermediate states (IM1 and IM2) among all repeats of each DMT. For the reverse bend (b), principal bend, transition, and straight regions, two, four, two, and five tomograms were included, respectively. Note that mildly bent flagella were mostly excluded from the histograms because of some ambiguity in assigning them to specific functional regions. The red arrows indicate the clustering of IM1 and IM2 conformations for IDAs a, g, and d in a bend direction–specific manner. For the distribution patterns, the conformations of the IDAs on the nine DMTs are schematically shown as individual grids; the grid colors represent the conformation of each inner dynein according to the color scheme in (B). In addition, a unique conformation of IDA g on DMT5 and the empty position of occasionally missing inner dyneins are indicated in light blue and gray, respectively. Scale bars are 20 nm in (A) and 10 nm in (B).

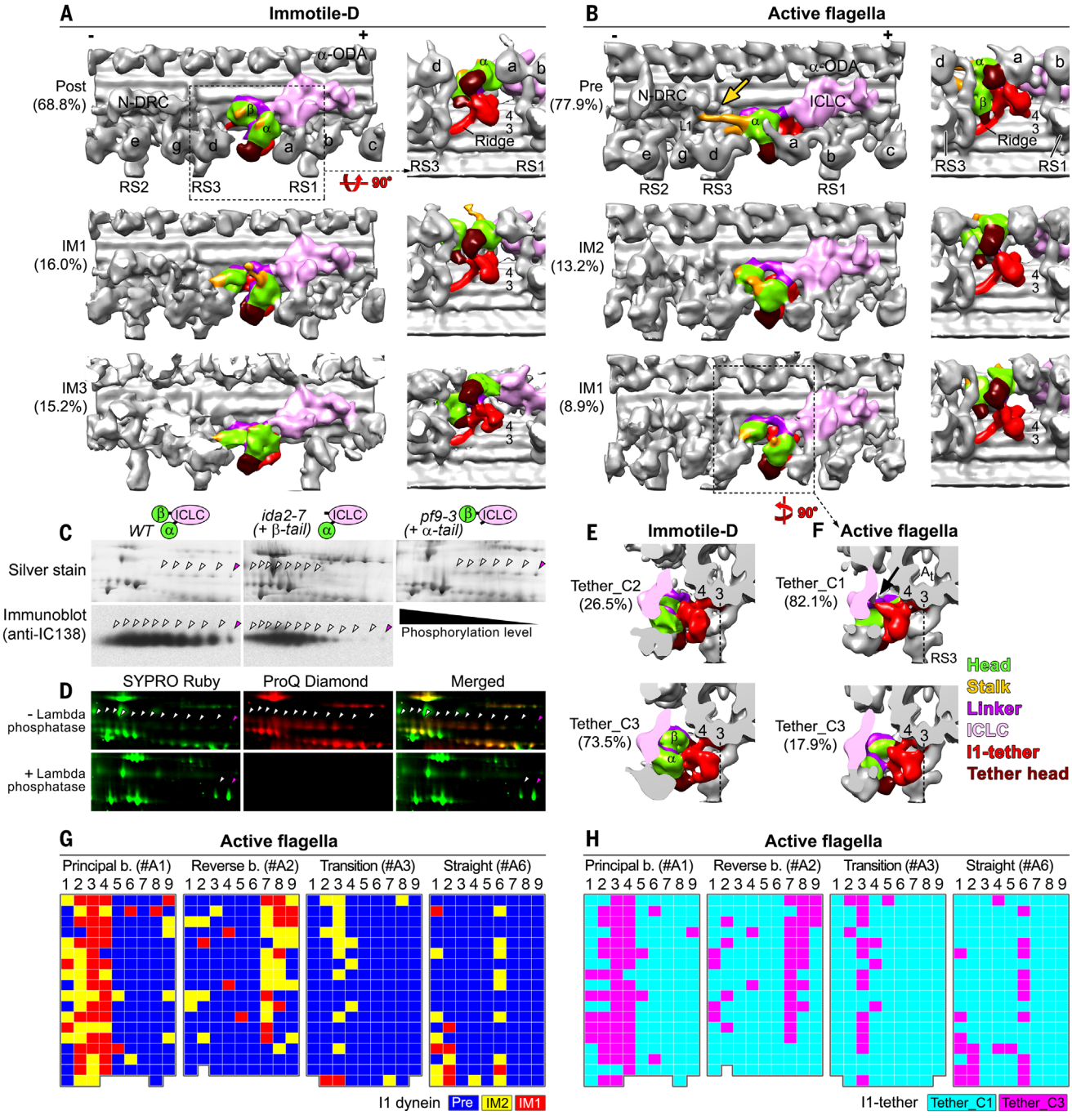

Fig. 5. The I1 dynein and I1-tether exhibit distinct and bend-correlated conformations in active flagella. (**A** and **B**) 3D isosurface renderings of the I1 dynein in the post–power stroke; intermediate IM1, IM2, and IM3; and pre–power stroke conformations in immotile-demembranated axonemes (A) and active flagella (B). Domain coloring is as shown in the legend in (F). Percentage of included subtomograms per class is indicated. a to e, and g indicate IDAs. The yellow arrow in (B) indicates the stalk of the pre–power stroke 1α-dynein. (**C**) 2D electrophoresis gels (top) and 2D immunoblots (bottom) of axonemal proteins show an increase in the phosphorylation of IC138 in *Chlamydomonas ida2-7*(+β-tail); note the higher abundance of highly phosphorylated isoforms on the acidic (left) side of the gels relative to isoforms with lower levels of phosphorylation. In WT and the *pf9-3*(+α-tail) mutant, IC138 exhibits a more evenly distributed string of spots (white and magenta arrowheads indicate the phosphorylated and nonphosphorylated isoforms of IC138, respectively). (**D**) Identification of phosphorylated IC138 isoforms in WT *Chlamydomonas* axonemes by 2D electrophoresis analysis. The six images show the spot pattern in the absence (top row) or presence (bottom row) of lambda phosphatase. Phosphorylated isoforms (white arrowheads) were detected by both total protein stain (SYPRO Ruby) and phosphoprotein stain (ProQ Diamond), whereas nonphosphorylated isoforms (magenta arrowheads) were only detected by total protein stain. (**E** and **F**) 3D isosurface renderings show the identified conformations of the I1-tether in immotile-demembranated (E) and active (F) flagella. Note the apparent interaction between the I1-tether (red) and I1-ICLC complex (light pink) in the tether_C1 conformation in active flagella (black arrow). Dashed lines serve as a reference to highlight the positional changes of the I1-tether. (**G** and **H**) Distributions of conformations of I1 dynein (G) and I1-tether (H) in different regions of active flagella. In (A), (B), and (E) to (H), flagella are from sea urchin sperm; in (C) and (D), flagella are from *Chlamydomonas*.

isoforms than the outer dyneins. This suggests that the fundamental roles of inner and outer dyneins during ciliary motility are distinct. For some, but not all, inner dynein isoforms, we observed some small clusters of intermediate conformations that were also in straight regions immediately neighboring significant bends, here called "transition" regions (Figs. 4C and 5G). We conclude that individual inner dynein isoforms likely play different roles in ciliary motility, including initiating flagellar bending in transition regions, preceding the conformational switching of the outer dyneins (Fig. 3C). This interpretation is consistent with genetic evidence from *Chlamydomonas* that suggests that inner dyneins are critical for waveform determination, whereas outer dyneins determine the power and speed of the bending. Thus, mutant flagella lacking inner dyneins display substantially reduced bend angles (*24*), which could be a result of defective bend initiation by inner dyneins a, g, d, and I1. By contrast, *Chlamydomonas* mutant flagella lacking outer dyneins are motile without considerable changes in waveform, but they exhibit reduced beat frequency (*25*). The conformational distributions of IDAs b, c, and e lacked obvious correlation with the bending direction, making these dynein isoforms likely not essential for bend initiation. However, they could still play roles in regulating flagellar waveform.

Potential regulatory mechanisms for conformational switching

Our study provides direct visualization of the asymmetric distribution of dynein activity and conformational switching between opposite sides of a beating flagellum. However, the nature of the switching signal(s) is still unknown. Four major models have been proposed for how the regular switching of dynein activity might be regulated, including (i) the distributor model, which proposes that a series of enzymatic and mechanical interactions between regulatory complexes [e.g., CPC, radial spokes, nexin-dynein regulatory complex (N-DRC), and I1 dynein] modulate dynein activity (*23*, *26*); (ii) the geometric clutch model, which posits that bending-induced distortions of the axoneme change the spacing between DMTs, acting as a "clutch" to disengage dyneins from their DMT tracks so that they can no longer generate force (or impede interdoublet sliding) (*27*); (iii) the sliding-control model, which postulates collective dynein behavior and a positive feedback mechanism in which the activity of dyneins leads to load-accelerated dissociation of dynein motors, meaning that the force per dynein head decreases as sliding velocity increases (*4*, *28*); and (iv) the curvature-control model, which hypothesizes that dynein's activity is regulated by local axonemal curvature, in that, when the axoneme is bent to a sufficient curvature, it triggers the activation of a different set of dyneins (*29*).

Our data reveal that not only dyneins but also major regulatory complexes display conformational switching in active flagella, which supports the distributor model (*26*). For example, both the regulatory I1 dynein and its associated I1-tether (*30*) undergo substantial conformational changes (Fig. 5, B and F) that correlate with the bend direction (Fig. 5, G and H), similar to IDAs a, g, and d.

We also observed previously undescribed attachments and dissociations between different regulators or regulators and dyneins, respectively. These conformational changes of regulators were spatially restricted in active flagella (for example, Fig. 5H), similar to specific activity states of the dyneins, and thus may represent the structural basis for transduction of regulatory signals. For example, the following four coordinated and bend direction–specific "connections" could allow for transient signal transduction between three major regulatory complexes: (i) the stalk of the pre–power stroke 1α-dynein (yellow arrow in Fig. 5B, pre, on left) connected to the proximally located nexin linker (part of the N-DRC); (ii) the stalk of pre–power stroke 1β-dynein (yellow in Fig. 5B, pre, on left) also projected proximally, but seemed to connect to IDA g and/or the base of radial spoke RS3; (iii) the head of pre–power stroke 1β-dynein (green in Fig. 5B, pre, on right) connected through the I1-tether and tether ridge (red in Fig. 5B, pre, on right) to the base of radial spoke RS3 (Fig. 5B, pre, on right, and movie S5); and (iv) the I1-tether in tether-class 1 (red in Fig. 5F, tether_C1) connected to the intermediate chain–light chain complex (ICLC, pink) of I1 dynein (Fig. 5F, arrow). The ICLC is known to be important for I1 docking and the regulatory function of I1 through its key regulatory component, the intermediate chain IC138, which is thought to be a "phosphor-switch" (*31*). These spatially restricted states of regulatory complexes and their interactions could be the structural basis for the conformational switching mechanisms seen for the dyneins during flagellar motility.

To further probe the possible functional importance of the I1 dynein motor domains for the regulation of switching of dynein activity, we tested the effect of the deletion of each of the I1 motor domains on the activity state of the regulatory subunit IC138. Knockout of either of the two I1 dynein HCs in *Chlamydomonas reinhardtii* results in mutant flagella (for example, mutants *ida2-7* and *pf9-3*) that lack the entire I1 dynein, including all ICLC subunits. However, transformation of these I1 mutants with just the tail fragment of the missing HC leads to partial rescue of the structural defects, in that all I1 subunits are present, except for the motor domain of the HC, which is still missing; specifically, mutant *pf9-3*(+α-tail) lacks the 1α-head (*32*) and mutant *ida2-7*(+β-tail) lacks the 1β-head (*33*) (Fig. 5C, cartoons). We found that IC138 is hyperphosphorylated in the mutant missing the 1β-HC motor domain [*ida2-7*(+β-tail)] but not in the mutant missing the 1α-HC motor domain [*pf9-3*(+α-tail)] (Fig. 5, C and D). Hyperphosphorylated IC138 was previously described as an "off" state that results in severe motility defects and the failure to regulate microtubule sliding in vitro (*31*, *34*). This highlights the importance of the 1β-HC motor domain for the regulation of ciliary motility.

Cross sections of active flagella show that the axoneme diameter and relative position of DMTs remain mostly the same in both bent and straight flagellar regions (Fig. 1G). However, between neighboring DMTs where the outer dyneins were in intermediate conformations in spatially restricted regions of active flagella, a small change was observed in the relative position of the DMTs, that is, here the neighboring doublet (DMT $n+1$) was located slightly lower (toward the axoneme center) (Fig. 2N, red arrows). This subtle, bend direction–dependent change in the relative positions of neighboring DMTs might be sufficient to disengage or weaken dynein's interaction with the neighboring DMT, either by increasing interdoublet distance or by decreasing the binding affinity of dynein to the DMT as a result of a changed angle between the dynein stalk and microtubule interface. Thus, our results are also consistent with the geometric clutch model (*27*).

In "paralyzed-flagella" mutants, the outer dyneins are active and in a tug-of-war

Our observation that, at steady state, most inner and outer dyneins in active flagella were in pre–power stroke conformations strongly suggests that axonemal dyneins are ready to bind ATP and undergo their mechanochemical cycle. So far, dyneins in paralyzed mutant flagella were assumed to be in their inactive post–power stroke state, as shown for axonemes deprived of ATP. Our data, however, suggest that dyneins in paralyzed mutants with defective regulators should still exhibit (mostly) primed pre– rather than post–power stroke conformations as long as ATP is present. Paralyzed flagella would therefore be immotile not because of a lack of dynein activity but because the tug-of-war between dyneins on opposite sides of the flagella results in balanced forces, similar to straight regions of active flagella.

The protein composition (*35*) and structure of axonemes are highly conserved across species (fig. S1B). For example, the loss of subunit DRC1 from the N-DRCs or of subunit RSP1 from the radial spokes results in similar motility defects in the green algae *Chlamydomonas* as in human primary ciliary dyskinesia patients (*36*, *37*). In addition, sea urchin sperm and *Chlamydomonas* flagella show comparable ATP-consumption rates during beating (*38*), suggesting that the molecular mechanism of flagellar motility is universally conserved. Therefore, we tested our hypothesis about the activity states of dyneins in paralyzed flagella by applying cryo-ET to readily available *Chlamydomonas pf19* flagella, which are paralyzed because of the absence of the CPC, a major regulatory complex of ciliary motility (*23*, *26*).

Indeed, in *pf19* flagella, the outer dyneins were predominantly in pre–power stroke conformations (Fig. 6, A to D), similar to the outer dyneins in active wild-type (WT) *Chlamydomonas* flagella (Fig. 6, E to H) and active sea urchin sperm flagella (Fig. 2, K to M). By contrast, the outer dyneins in control flagella—that is, ATP-free isolated *Chlamydomonas* WT flagella and pseudo-WT (pWT) axonemes—were in the post–power stroke conformation (Fig. 6, I to P). Most paralyzed flagellar mutants, including *pf19*, can undergo dynein-driven sliding disintegration, that is, linear DMT

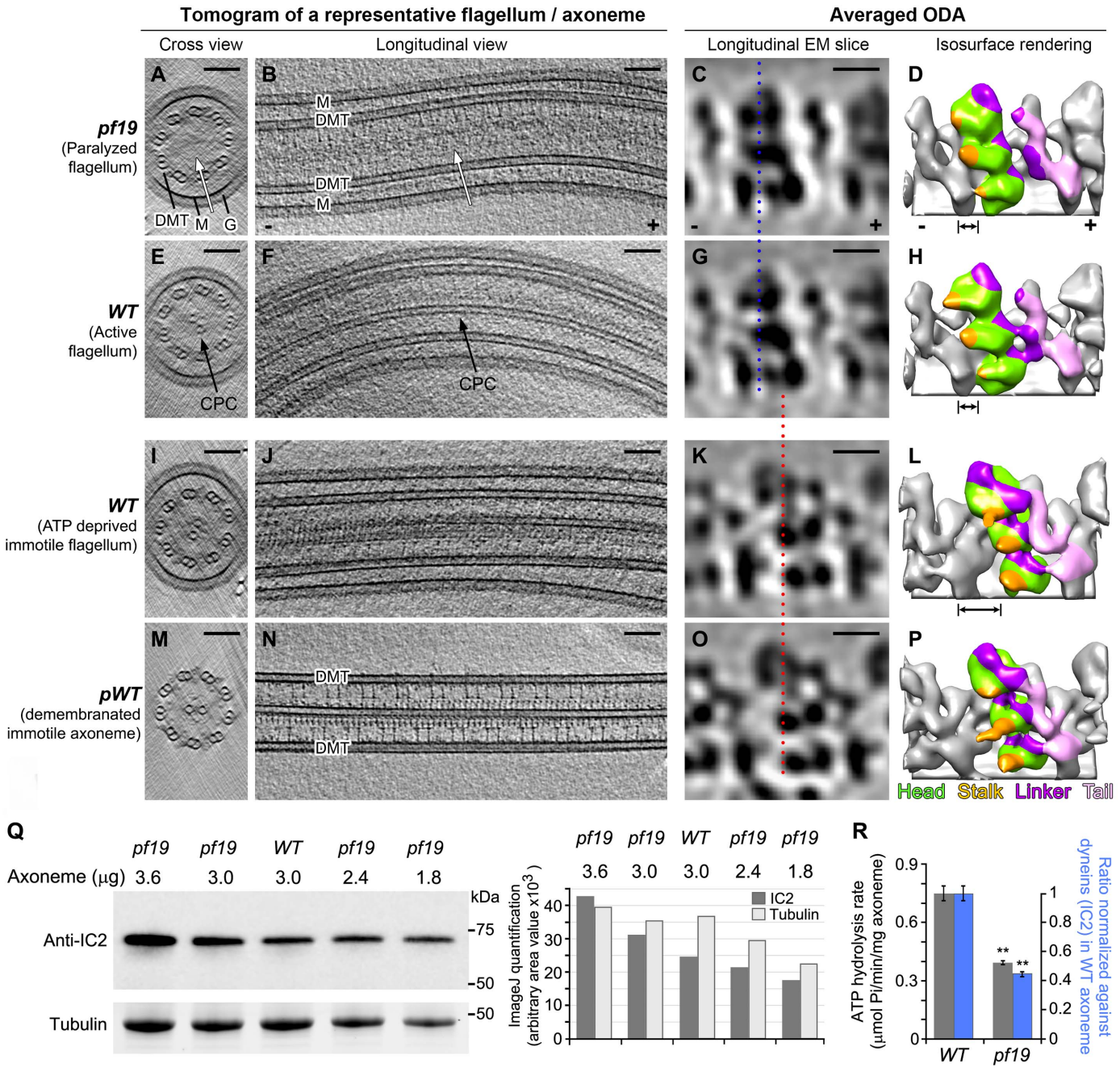

Fig. 6. Outer dyneins in paralyzed *pf19* mutant flagella from *Chlamydomonas* are in pre–power stroke conformations. (**A** to **P**) Representative tomograms and averaged ODAs in the following *Chlamydomonas* samples: paralyzed flagella of intact *pf19* cells (white arrow indicates missing CPC) [(A) to (D)], active flagella from intact WT cells [(E) to (H)], detached immotile WT flagella without ATP [(I) to (L)], and immotile-demembranated axonemes from rescued pWT strain (*pf2-4; PF2::GFP*) [(M) to (P)]. Note that the intact flagellar membrane (indicated by M) is surrounded by a dense glycocalyx (indicated by G) layer, resulting in thicker samples and noisier tomograms compared to demembranated axonemes in (M) and (N). The averaged outer dyneins in both paralyzed *pf19* and active WT flagella were predominantly in their pre–power stroke conformations, with the three dynein motor heads (green) and stalks (orange) closer to the microtubule minus end [(C), (D), (G), and (H)] as compared to the post–power stroke conformation observed in immotile detached and demembranated flagella [(K), (L), (O), and (P)]. The blue and red dotted lines along the proximal edge of the bottom dynein head [in (C), (G), (K), and (O)] and the double-headed arrows [in (D), (H), and (L)] facilitate comparison of the head positions. (**Q**) Comparison of the relative abundance of the ODA intermediate chain IC2 in WT and *pf19* axoneme samples by immunoblot analysis (left) and densitometry quantification of the bands (right). The abundance of IC2 in *pf19* axonemes was 1.19 ± 0.03 times that in WT axonemes due to the missing CPC proteins in *pf19*. Tubulin is a loading control (but note that the ratio between tubulin and total protein mass is slightly changed in the mutant). (**R**) ATP hydrolysis rate of WT and *pf19* axonemes (bar chart shows means ± SD, $n = 3$; $^{**}P < 0.01$; Student's t test). For the same amount of axonemes, the ATPase activity of *pf19* is 0.53 ± 0.02 that of WT (gray bars), and, after accounting for the amount of dyneins and normalizing against WT, the ATPase activity of *pf19* is significantly lower, 0.44 ± 0.02 that of WT (blue bars). Scale bars are 100 nm in (A), (B), (E), (F), (I), (J), (M), and (N) and 10 nm in (C), (G), (K), and (O).

extrusion, after proteolytic cleavage of interdoublet linkers and addition of ATP (*23*). This confirms that the pre–power stroke outer dyneins in *pf19* observed here require only ATP, rather than additional activating signals, to induce interdoublet sliding.

The observed prevalence of pre–power stroke dyneins in intact beating sea urchin sperm flagella, and in WT and paralyzed mutant *Chlamydomonas* flagella (Figs. 2 to 6), can be partially explained by previous kinetic studies that have indicated that, in the dynein ATPase cycle, the power stroke and release of adenosine diphosphate (ADP) (that is, the prestroke-to-poststroke transition) are the rate-limiting steps, whereas the recovery stroke (poststroke-to-prestroke transition) proceeds rapidly, about 1000 times faster (*39*). However, other mechanisms preventing the primed dyneins from completing their power stroke could also contribute. For example, previous optical trap experiments demonstrated that dynein's detachment rate decreases with increasing opposing load, that is, dynein binds tighter to microtubules when a force is applied on the dynein tail that is directed toward the plus end of the microtubule (*40*, *41*). In flagella, the activity of dyneins on opposite sides of the axoneme would cause opposing directions of interdoublet sliding, which would be perceived by the respective dyneins as a load increase (a force exerted on the dynein tails directed toward the microtubule plus end). Thus, simultaneously active dyneins on opposite sides of the axoneme could cause tighter microtubule binding or even catch bond of these dyneins. The tension applied by means of the tail domain and allosteric interhead communication between neighboring motor domains of the dimeric ODAs could prevent the primed dyneins from completing their power stroke (*7*).

The prevalence of pre–power stroke dyneins in beating and paralyzed mutant flagella (Figs. 2 to 6), together with the dynein distribution patterns that agree well with the prevailing notion of bend generation (fig. S2D) and the switch-point hypothesis (*13*), strongly suggests that, at steady state, dyneins in cilia are in an active state by default and ready to undergo a mechanochemical cycle, without requiring specific activating signals, as long as ATP is present. These direct structural findings are consistent with previous biochemical studies, such as DMT extrusion from protease-treated WT and mutant axonemes, and motility assays of isolated dyneins (*12*, *22*, *23*). It therefore follows that, for flagellar bending to occur, proper regulatory signals are required to reduce dynein activity on one side of the flagellum to generate the force imbalance required to bend the flagellum. In the absence of such inhibitory signals, the dynein forces generated on opposite sides are balanced, resulting in "rigor" paralyzed flagella.

Although the outer dyneins in *pf19* flagella were predominantly in pre–power stroke conformations, we hypothesized that the tug-of-war between opposite sides of the flagellum could prevent the dynein power stroke and keep many dyneins in their primed pre-II states, thus preventing futile ATP hydrolysis. This is supported by our comparative measurement of ATP consumption by isolated axonemes from WT and *Chlamydomonas pf19* flagella; the ATP hydrolysis rate of *pf19* axonemes is less than half (44%) that of WT axonemes (Fig. 6, Q and R).

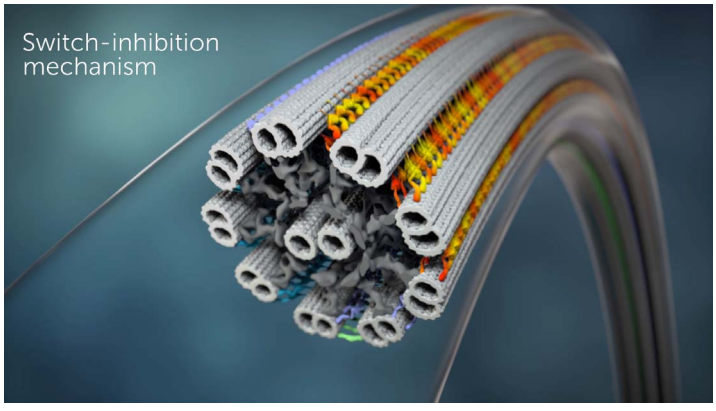

Movie 1. Switch-inhibition mechanism. The animation summarizes the switch-inhibition mechanism of ciliary and flagellar beating, as suggested by our cryo-ET study of active sea urchin sperm flagella. Note that the depicted durations of different conformational states of dyneins do not reflect the native kinetics of the molecules.

"Switch-inhibition" model

Our direct analysis of the spatial regulation of dynein activity revealed three tenets that are important for dynein-driven flagellar motility: (i) The asymmetric distribution of dynein activity results in unidirectional bending, (ii) the switching of dynein conformations between opposite sides of the flagellum causes the undulating waveform of beating flagella, and (iii) at steady state, dyneins are in the active pre–power stroke states, and the asymmetry of dynein activity is most likely caused by selectively inhibiting dyneins on one side of the flagellum. Given that bends are usually initiated at the flagellar base and travel over time to the tip, the spatially restricted and cooperative conformational changes seen along frozen flagella likely also represent the temporal sequence of structural changes during wave formation. By correlating structural changes with their locations in the flagellar bend, we are able to propose the following switch-inhibition model, in which ciliary and flagellar motility is generated by inhibiting, rather than activating, dyneins on alternating sides of the flagellum (Fig. 7 and Movie 1):

1) Straight regions: Under physiological conditions (ATP present) and with the regulators in their off state or the inhibitory signal still below a threshold, the dynein forces on opposite sides of the flagellum are counterbalanced, keeping the flagellum straight (Figs. 7, third cross section from the top, and 3C, straight). Without proper function of regulators that can "break" the force balance, such as what occurs in the *pf19* mutant, flagella appear paralyzed and stiff.

2) Bend initiation: Regulatory signals lead first to the inhibition of inner dyneins (for example, dyneins a, g, d, and I1) either on DMTs 2 to 4 (for principal bend) or DMTs 7 to 9 (for reverse bend) (Figs. 7, fourth cross section from the top, and 4C and 5G, transition). When enough inner dyneins are inhibited on one side, dyneins on the opposite side can begin to exert a net force sufficiently strong enough to initiate a mild bend in the flagellum.

3) Bending: The positional changes of DMTs caused by the mild bend initiation and/or transduction of the inhibitory signal downstream to the outer dyneins on the inhibited side of the axoneme allow for a rapid increase of net bending force generated by the active dyneins on the opposite side of the flagellum. This causes further interdoublet sliding, which is restricted by the basal body and molecular interdoublet links, causing a full bend of the flagellum in one direction, that is, the principal or the reverse bend (Figs. 7, first and fifth cross sections, and 3C, principal and reverse bend regions of active flagella).

After the inhibitory signals are turned off by as-yet-unknown trigger(s), dynein activity on the previously inhibited side recovers, causing the flagellum to straighten (Figs. 7, second cross section from the top, and 4C and 5G, transition) and the bending cycle restarts. By switching the side of dynein inhibition in regular time intervals, the flagellum alternates the direction of bending, resulting in the typical planar waveform of sea urchin sperm flagella.

Switch inhibition is a robust mechanism

Although the original switch-point hypothesis (*13*) did not specify the regulatory mechanism that underlies the asymmetric distribution of dynein activity, data interpretation in the field focused mainly on active sliding and dynein activation. Our switch-inhibition model provides a comprehensive molecular mechanism for flagellar beat generation that appears more robust than the previously assumed switch-activation model. Flagella beat over a long time with fairly consistent waveform, amplitude, and beat frequency of 50 to 60 Hz, that is, the bending direction switches rapidly every ~10 ms. However, as with a switch-activation mechanism, the regulators would have to activate dyneins in a spatiotemporally coordinated manner with high efficiency,

and the bend amplitude would directly depend on the number of synchronously activated dyneins.

By contrast, a switch-inhibition mechanism could happen in an "all-or-none" fashion. Indeed, the spatially restricted inhibition of just a fraction of the dyneins would be sufficient to cause cooperative microtubule release of all dyneins on the inhibited flagellar side, allowing the predominantly active dyneins on the opposite side to rapidly drive bending. The advantage of the all-or-none principle is that the strength of a response can be independent of the strength of the input signal. As long as the inhibitory signal exceeds a specific threshold (for example, a minimum number of inhibited dyneins), the flagellum would bend consistently with 100% wave amplitude, resulting in the relatively constant and sustained beating of cilia and flagella. All-or-none mechanisms are often observed in cellular processes that require rapid switching and/or preservation of signal strength, such as transduction of action potentials and heart-muscle contraction (*42*, *43*). Our findings will guide future interpretations and shift the field's focus to molecular mechanisms underpinning the spatiotemporally coordinated inactivation of dyneins.

Materials and methods

Sample preparation

Spawning of male adult sea urchins (*Strongylocentrotus purpuratus* purchased from Monterey Abalone, Monterey, CA) was induced by the injection of 1 to 2 ml of 0.5 M KCl into the perivisceral cavity. Sperm samples were collected and a small aliquot was diluted in artificial seawater (360 mM NaCl, 50 mM $MgCl_2$, 10 mM $CaCl_2$, 10 mM KCl, and 30 mM HEPES, pH 8.0) to examine the motility by light microscopy using the differential interference contrast (DIC) mode of a Marianas spinning disk confocal system (3I, Denver, CO) consisting of a Zeiss Axio Observer Z1 microscope (Carl Zeiss, Jena, Germany) equipped with a Yokogawa CSU-X1 spinning disk confocal head (Yokogawa, Tokyo, Japan) and a QuantEM 512SC EMCCD camera (Photometrics, Tucson, AZ). All harvested sperm cells were motile (movie S1), and the samples were then divided to prepare three different types of samples: (part A) active flagella, (part B) ATPase-inhibited immotile flagella (immotile-I), and (part C) demembranated immotile axonemes (immotile-D). Part A was diluted in artificial seawater and rapidly frozen (as described below). Part B was diluted in artificial seawater containing the ATPase inhibitor erythro-9-(2-hydroxy-3-nonyl)adenine hydrochloride (EHNA hydrochloride, 2 mM; Santa Cruz Biotechnology) (*44*); after incubation for 5 min, we confirmed by light microscopy that the sperm were completely immotile (movie S2) and then rapidly froze the sample. Part C was diluted in demembranation buffer (30 mM HEPES pH 8.0, 150 mM KCl, 4 mM $MgCl_2$, 0.5 mM EGTA, and 0.1% Triton X-100) to remove the flagellar membrane (but axonemes remained attached to the cell body). After incubation for 1 min, the sperm were collected by centrifugation at 1000*g*, resuspended in demembranation buffer (but without Triton X-100), and rapidly frozen.

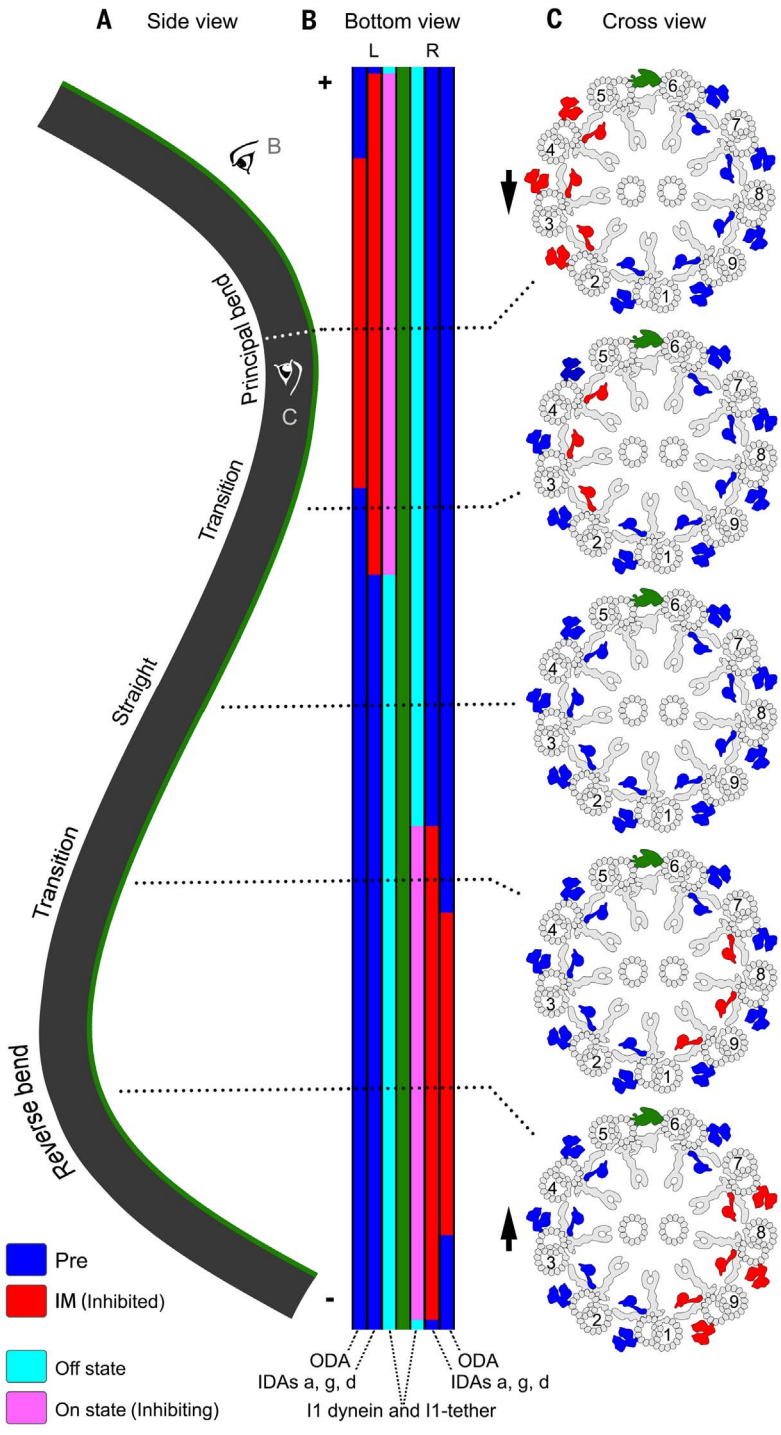

Fig. 7. Schematic model of the switch-inhibition mechanism of ciliary and flagellar motility. (**A** to **C**) Summary illustration of a sinusoidal wave of an active flagellum that contains reverse bend, transition, straight, and principal bend regions. The schematic shows the flagellum in different views: longitudinal views from its "left" side (where DMTs 2 to 4 are located) (A), as viewed from the bottom passing through the o-SUB5-6 bridge and DMT1 (L and R indicate the left and right sides of the flagellum) (B), and cross-sectional views from the proximal end (C). The view directions of (B) and (C) are indicated in (A) by their corresponding letters. In (B) and (C), the distributions of the different activity states of the dyneins and the I1-tether (as indicated below the bottom view) are shown in the different functional regions of the flagellum. The different states are indicated by distinct colors (as specified in the color legend at the bottom left). Note that the flagellar wave travels from the proximal base (minus end) to the distal tip (plus end) of the flagellum; this means that the functional state shown, for example, in the fourth cross section from the top (transition and bend initiation) precedes the state shown in the fifth cross section (reverse bend) in time.

Chlamydomonas reinhardtii strains used in this study include WT (wild-type strain: CC-125, 137c mt+), pWT (a pseudo-WT strain: *pf2-4; PF2::GFP*) (*9*), a CPC-lacking mutant *pf19* (strain: cc-1037 mt+) (*23*), and two I1 dynein mutant strains: *pf9-3*(+α-tail) (strain: *pf9-3; pf9-3::G41a*) and *ida2-7*(+β-tail) (strain: *ida2-7; ida2-7::pCAP1*). The *pf9-3*(+α-tail) and *ida2-7*(+β-tail) strains lack the motor domains of 1α- and 1β-HC, respectively (*32*, *33*). *Chlamydomonas* cells were grown in liquid Tris acetate-phosphate medium at room temperature with a light:dark cycle of 16:8 hours. Axonemes were isolated from *Chlamydomonas reinhardtii* cells as previously described (*30*). Briefly, flagella were detached from the cells using the pH-shock method and purified by two centrifugation steps over 20% sucrose cushions. Purified flagella were demembranated with 1% IGEPAL CA-630 (Sigma-Aldrich, St. Louis, MO), and axonemes were collected by centrifugation at 10,000*g* for 10 min. Except for WT and *pf19* axonemes that were used for an ATPase assay and pWT axonemes that were used for cryo-ET analysis, the axoneme pellet was directly dissolved in two-dimensional electrophoresis (2DE) lysis buffer [7 M urea, 2 M thiourea, 4% (wt/wt) CHAPS, 65 mM DTT, and 2% (vol/vol) IPG buffer (pH 3-10NL; GE Healthcare)] by vigorously stirring for 0.5 hours. Cell debris and insoluble material were removed by centrifugation at 45,000*g* for 1 hour. The supernatant was aliquoted and stored at −70°C until subsequent analysis.

For the phosphorylation analysis of IC138, the protein samples dissolved in 2DE lysis buffer were precipitated using the 2-D Clean-Up Kit (GE Healthcare) and resuspended in Milli-Q water to approximately 4 mg/ml. Phosphatase treatment using Lambda Protein Phosphatase was performed as previously described (*45*). Briefly, two 85-μl aliquots of the protein sample were mixed with 10 μl of 10% SDS and were vigorously vortexed for 20 s, followed by the addition of 695 μl of Milli-Q water, 100 μl of 10 mM $MnCl_2$, 100 μl of 10× Lambda Protein Phosphatase buffer (New England Biolabs), and 10 μl of protease inhibitor cocktail (P9599, Sigma-Aldrich). To one of the two aliquots, 1200 units of Lambda Protein Phosphatase (New England Biolabs) was added, and both aliquots were then incubated overnight at 30°C. Phosphatase-treated and untreated protein samples were precipitated using acetone (−20°C), resuspended in 2DE lysis buffer, further purified using the 2-D Clean-Up Kit (GE Healthcare), and resuspended in 2DE lysis buffer to a final concentration of approximately 4 mg/ml.

Cryo-sample preparation and cryo-ET

Cryo-samples were prepared, imaged by cryo-ET, and processed as previously described (*17*). Briefly, Quantifoil holey carbon grids (Quantifoil Micro Tools GmbH, Germany) were glow discharged, coated with 10-nm gold (Sigma-Aldrich), and loaded onto a homemade plunge-freezing device. Three microliters of sample [that is, actively swimming sea urchin sperm cells, *Chlamydomonas* WT cells, immotile sea urchin sperm cells (demembranated or treated with EHNA), paralyzed *Chlamydomonas pf19* cells, isolated *Chlamydomonas* WT flagella or pWT axonemes, respectively] and 1 μl of fivefold concentrated BSA coated 10-nm colloidal gold solution were applied to the grid, blotted with filter paper for 1.5 to 2.5 s, and immediately plunge-frozen in liquid ethane. Vitrified specimens were transferred into a Tecnai F30 transmission electron microscope (FEI, Hillsboro, OR) with a cryo-holder (Gatan, Pleasanton, CA). Flagella and/or axonemes that appeared well preserved by EM inspection were imaged at 300 keV, with −6- or −8-μm defocus, under low-dose conditions and using an energy filter in zero-loss mode (Gatan, Pleasanton, CA) (20-eV slit width). Tilt series were recorded while stepwise rotating the sample from about −65° to +65° with 1.5° to 2.5° increments using the microscope control software SerialEM (*46*). The cumulative electron dose per tilt series was limited to approximately 100 $e/Å^2$. All images were digitally recorded on a 2k×2k charge-coupled device camera (Gatan, Pleasanton, CA) at a nominal magnification of 13,500, resulting in a pixel size of approximately 1 nm.

Image processing

The tilt series images were reconstructed into 3D tomograms by weighted back projection using the IMOD software package (*47*). Some tomograms were previously utilized for the analysis of axonemal dyneins (*17*). Only tomograms of intact and noncompressed flagella and/or axonemes were used for further data analysis. To enhance the signal-to-noise ratio and improve the resolution, subtomograms that contained the 96-nm axonemal repeat units along the doublet microtubules (volume size: 110 nm by 84 nm by 80 nm) or that contained individual ODAs (volume size: 56 nm by 56 nm by 56 nm) were extracted from the raw tomograms, aligned, and averaged (including missing wedge compensation) using the PEET program to obtain subtomogram averages (*18*). To identify distinct conformations of various axonemal structures, classification analyses were performed on the aligned subtomograms using a clustering approach (principal component analysis) built into the PEET program (*19*). Before classification, appropriate masks were applied to focus the classification on structures of interest. Subtomograms that contained the structure of interest with an identical conformation were grouped into a class, and were averaged to generate a class average. The automatic classification into different conformational states of axonemal complexes was performed by an automated algorithm without prior knowledge about from which functional region of a flagellar wave individual subtomograms were extracted. Using the information provided by the classification analysis, we then mapped the conformational state of each subtomogram and/or repeat back onto the respective location in the raw tomograms. The numbers of tomograms and subtomograms analyzed by classification are summarized in table S1. The resolution of the resulting averages was estimated in a $(30\ nm)^3$ subvolume in the center of the structure of interest using the Fourier shell correlation method with a criterion of 0.5 (*48*). The structures were visualized as 2D tomographic slices and 3D isosurface renderings using IMOD (*47*) and UCSF Chimera (*49*), respectively.

Electrophoresis and phosphorylation analysis

2DE analysis was performed as previously described (*45*). Briefly, *Chlamydomonas* axonemal proteins (70 μg) were separated in the first dimension on 13-cm immobilized pH 3-10NL IPG strips (GE Healthcare) for 24 kVh, followed by 10% SDS-PAGE for the second dimension. All samples (two to seven samples for each strain) were run in at least duplicate to confirm reproducibility. To visualize total proteins, the gels were stained with silver nitrate; to visualize phosphoproteins, the gels were stained with Pro-Q Diamond Phosphoprotein Gel Stain (Thermo Fisher Scientific) according to the manufacturer's instructions. After image acquisition using a Typhoon 9410 Variable Mode Imager (GE Healthcare), the Pro-Q Diamond-stained gels were poststained with SYPRO Ruby Protein Gel Stain (Thermo Fisher Scientific) to detect total protein.

Immunoblot

For 2D immunoblot analysis of IC138, 35 μg of total axonemal proteins was separated by 2DE with 7-cm immobilized pH 3-10NL IPG strips (GE Healthcare) for the first dimension and 10% SDS-PAGE gels for the second dimension. Immunoblot analysis was performed using a polyclonal IC138 antibody (1:10,000) (*31*). Signals were visualized using the ECL detection system (Bio-rad).

For immunoblot analysis of ODA IC2 protein, the axonemal proteins were resolved by SDS-PAGE on Any kD TGX Strain-FreeTM protein gels (Bio-rad Cat# 4568123). After visualizing by ChemiDocTM Touch Imaging System (Bio-Rad), proteins were blotted onto PVDF membranes (Bio-Rad) and probed with anti-IC2 monoclonal antibody (Sigma-Aldrich, D6168; 1:5000). Signals were visualized using the ECL detection system (Bio-rad), and quantified by ImageJ software.

ATPase assay and analysis of relative ATP consumption

The rate of phosphate release by ATP hydrolysis of axonemes was measured in bulk as described before (*50*). Briefly, isolated axonemes were washed and resuspended in HMEEK buffer (30 mM Hepes, pH 7.4, 5 mM $MgSO_4$, 1 mM EGTA, 0.1 mM EDTA, and 25 mM KCl). 150 μl of axonemes (10.3 μg) were incubated with 1.3 μl of 50 mM ATP (resulting in 0.43 mM ATP in solution) for 1 min. The ATP hydrolysis was stopped by adding 150 μl of 12% SDS solution. Color was developed by incubation with 300 μl of a 1:1 solution of 6% ascorbic acid in 1 N HCl and 1% $(NH_4)_6Mo_7O_{24}.4H_2O$ in 12% SDS for 10 min and was stopped by adding 450 μl of 2% sodium citrate, 2% $NaAsO_2$, and 2% acetic acid followed by 20 min incubation at room temperature. The concentrations of the released phosphate were calculated from the color absorbance at 850 nm. The relative abundance of the ODA intermediate

chain protein IC2 in WT and *pf19* axoneme was used to correlate total protein amount to number of dynein molecules (more dyneins per total protein in *pf19* because of lack of CPC). The densitometry quantification of the IC2 Western blot bands was performed by ImageJ software (Fig. 6Q). On the basis of analyses of three independent samples, the abundance of IC2 in *pf19* axoneme was 1.19 ± 0.03 times higher than that in WT axonemes (Fig. 6Q). For the same amount of axonemes, the ATPase activity of *pf19* is 0.53 ± 0.02 of that of WT. As the abundance of dyneins in *pf19* axonemes is 1.19 times that in WT axonemes, the ATPase activity of *pf19* is 0.44 ± 0.02 of that of WT after accounting for the amount of dyneins and normalizing against WT (Fig. 6R). The data were analyzed by Student's *t* test.

REFERENCES AND NOTES

1. Cilia and flagella share the same conserved structure and differ only in waveform and/or length; therefore, the terms "cilia" and "flagella" are often used interchangeably, including in this paper.
2. H. M. Mitchison, E. M. Valente, Motile and non-motile cilia in human pathology: From function to phenotypes. *J. Pathol.* **241**, 294–309 (2017). doi: 10.1016/j.jmb.2012.05.040; pmid: 22683354
3. N. Mizuno, M. Taschner, B. D. Engel, E. Lorentzen, Structural studies of ciliary components. *J. Mol. Biol.* **422**, 163–180 (2012). doi: 10.1016/j.jmb.2012.05.040; pmid: 22683354
4. T. J. Mitchison, H. M. Mitchison, Cell biology: How cilia beat. *Nature* **463**, 308–309 (2010). doi: 10.1038/463308a; pmid: 20090745
5. M. Kikkawa, Big steps toward understanding dynein. *J. Cell Biol.* **202**, 15–23 (2013). doi: 10.1083/jcb.201304099; pmid: 23836927
6. I. R. Gibbons, A. J. Rowe, Dynein: A protein with adenosine triphosphatase activity from cilia. *Science* **149**, 424–426 (1965). doi: 10.1126/science.149.3682.424; pmid: 17809406
7. H. Schmidt, A. P. Carter, Review: Structure and mechanism of the dynein motor ATPase. *Biopolymers* **105**, 557–567 (2016). doi: 10.1002/bip.22856; pmid: 27062277
8. P. Höök, R. B. Vallee, The dynein family at a glance. *J. Cell Sci.* **119**, 4369–4371 (2006). doi: 10.1242/jcs.03176; pmid: 17074830
9. J. Lin, T. Heuser, K. Song, X. Fu, D. Nicastro, One of the nine doublet microtubules of eukaryotic flagella exhibits unique and partially conserved structures. *PLOS ONE* **7**, e46494 (2012). doi: 10.1371/journal.pone.0046494; pmid: 23071579
10. R. Kamiya, T. Yagi, Functional diversity of axonemal dyneins as assessed by in vitro and in vivo motility assays of *Chlamydomonas* mutants. *Zool. Sci.* **31**, 633–644 (2014). doi: 10.2108/zs140066; pmid: 25284382
11. W. S. Sale, P. Satir, Direction of active sliding of microtubules in *Tetrahymena* cilia. *Proc. Natl. Acad. Sci. U.S.A.* **74**, 2045–2049 (1977). doi: 10.1073/pnas.74.5.2045; pmid: 266725
12. K. E. Summers, I. R. Gibbons, Adenosine triphosphate-induced sliding of tubules in trypsin-treated flagella of sea-urchin sperm. *Proc. Natl. Acad. Sci. U.S.A.* **68**, 3092–3096 (1971). doi: 10.1073/pnas.68.12.3092; pmid: 5289252
13. J. Wais-Steider, P. Satir, Effect of vanadate on gill cilia: Switching mechanism in ciliary beat. *J. Supramol. Struct.* **11**, 339–347 (1979). doi: 10.1002/jss.400110309; pmid: 120905
14. S. Hayashi, C. Shingyoji, Mechanism of flagellar oscillation-bending-induced switching of dynein activity in elastase-treated axonemes of sea urchin sperm. *J. Cell Sci.* **121**, 2833–2843 (2008). doi: 10.1242/jcs.031195; pmid: 18682495
15. W. S. Sale, The axonemal axis and Ca^{2+}-induced asymmetry of active microtubule sliding in sea urchin sperm tails. *J. Cell Biol.* **102**, 2042–2052 (1986). doi: 10.1083/jcb.102.6.2042; pmid: 2940250
16. S. L. Tamm, S. Tamm, Alternate patterns of doublet microtubule sliding in ATP-disintegrated macrocilia of the ctenophore *Beroë*. *J. Cell Biol.* **99**, 1364–1371 (1984). doi: 10.1083/jcb.99.4.1364; pmid: 6480696
17. J. Lin, K. Okada, M. Raytchev, M. C. Smith, D. Nicastro, Structural mechanism of the dynein power stroke. *Nat. Cell Biol.* **16**, 479–485 (2014). doi: 10.1038/ncb2939; pmid: 24727830
18. D. Nicastro *et al.*, The molecular architecture of axonemes revealed by cryoelectron tomography. *Science* **313**, 944–948 (2006). doi: 10.1126/science.1128618; pmid: 16917055
19. J. M. Heumann, A. Hoenger, D. N. Mastronarde, Clustering and variance maps for cryo-electron tomography using wedge-masked differences. *J. Struct. Biol.* **175**, 288–299 (2011). doi: 10.1016/j.jsb.2011.05.011; pmid: 21616153
20. K. Zhang *et al.*, Cryo-EM reveals how human cytoplasmic dynein is auto-inhibited and activated. *Cell* **169**, 1303–1314.e18 (2017). doi: 10.1016/j.cell.2017.05.025; pmid: 28602352
21. B. I. Carbajal-González *et al.*, Conserved structural motifs in the central pair complex of eukaryotic flagella. *Cytoskeleton (Hoboken)* **70**, 101–120 (2013). doi: 10.1002/cm.21094; pmid: 23281266
22. T. Kon, T. Mogami, R. Ohkura, M. Nishiura, K. Sutoh, ATP hydrolysis cycle-dependent tail motions in cytoplasmic dynein. *Nat. Struct. Mol. Biol.* **12**, 513–519 (2005). doi: 10.1038/nsmb930; pmid: 15880123
23. G. B. Witman, J. Plummer, G. Sander, *Chlamydomonas* flagellar mutants lacking radial spokes and central tubules. Structure, composition, and function of specific axonemal components. *J. Cell Biol.* **76**, 729–747 (1978). doi: 10.1083/jcb.76.3.729; pmid: 632325
24. C. J. Brokaw, R. Kamiya, Bending patterns of *Chlamydomonas* flagella: IV. Mutants with defects in inner and outer dynein arms indicate differences in dynein arm function. *Cell Motil. Cytoskeleton* **8**, 68–75 (1987). doi: 10.1002/cm.970080110; pmid: 2958145
25. D. R. Mitchell, J. L. Rosenbaum, A motile *Chlamydomonas* flagellar mutant that lacks outer dynein arms. *J. Cell Biol.* **100**, 1228–1234 (1985). doi: 10.1083/jcb.100.4.1228; pmid: 3156867
26. E. F. Smith, P. Yang, The radial spokes and central apparatus: Mechano-chemical transducers that regulate flagellar motility. *Cell Motil. Cytoskeleton* **57**, 8–17 (2004). doi: 10.1002/cm.10155; pmid: 14648553
27. C. B. Lindemann, A "geometric clutch" hypothesis to explain oscillations of the axoneme of cilia and flagella. *J. Theor. Biol.* **168**, 175–189 (1994). doi: 10.1006/jtbi.1994.1097
28. I. H. Riedel-Kruse, A. Hilfinger, J. Howard, F. Jülicher, How molecular motors shape the flagellar beat. *HFSP J.* **1**, 192–208 (2007). doi: 10.2976/1.2773861; pmid: 19404446
29. P. Sartori, V. F. Geyer, A. Scholich, F. Jülicher, J. Howard, Dynamic curvature regulation accounts for the symmetric and asymmetric beats of *Chlamydomonas* flagella. *eLife* **5**, e13258 (2016). doi: 10.7554/eLife.13258; pmid: 27166516
30. T. Heuser *et al.*, Cryoelectron tomography reveals doublet-specific structures and unique interactions in the I1 dynein. *Proc. Natl. Acad. Sci. U.S.A.* **109**, E2067–E2076 (2012). doi: 10.1073/pnas.1120690109; pmid: 22733763
31. R. Bower *et al.*, IC138 defines a subdomain at the base of the I1 dynein that regulates microtubule sliding and flagellar motility. *Mol. Biol. Cell* **20**, 3055–3063 (2009). doi: 10.1091/mbc.E09-04-0277; pmid: 19420135
32. S. H. Myster, J. A. Knott, K. M. Wysocki, E. O'Toole, M. E. Porter, Domains in the 1α dynein heavy chain required for inner arm assembly and flagellar motility in Chlamydomonas. *J. Cell Biol.* **146**, 801–818 (1999). doi: 10.1083/jcb.146.4.801; pmid: 10459015
33. C. A. Perrone, S. H. Myster, R. Bower, E. T. O'Toole, M. E. Porter, Insights into the structural organization of the I1 inner arm dynein from a domain analysis of the 1β dynein heavy chain. *Mol. Biol. Cell* **11**, 2297–2313 (2000). doi: 10.1091/mbc.11.7.2297; pmid: 10888669
34. S. Toba *et al.*, Distinct roles of 1α and 1β heavy chains of the inner arm dynein I1 of *Chlamydomonas* flagella. *Mol. Biol. Cell* **22**, 342–353 (2011). doi: 10.1091/mbc.E10-10-0806; pmid: 21148301
35. G. J. Pazour, N. Agrin, J. Leszyk, G. B. Witman, Proteomic analysis of a eukaryotic cilium. *J. Cell Biol.* **170**, 103–113 (2005). doi: 10.1083/jcb.200504008; pmid: 15998802
36. M. Wirschell *et al.*, The nexin-dynein regulatory complex subunit DRC1 is essential for motile cilia function in algae and humans. *Nat. Genet.* **45**, 262–268 (2013). doi: 10.1038/ng.2533; pmid: 23354437
37. J. Lin *et al.*, Cryo-electron tomography reveals ciliary defects underlying human *RSPH1* primary ciliary dyskinesia. *Nat. Commun.* **5**, 5727 (2014). doi: 10.1038/ncomms6727; pmid: 25473808
38. D. T. Chen, M. Heymann, S. Fraden, D. Nicastro, Z. Dogic, ATP consumption of eukaryotic flagella measured at a single-cell level. *Biophys. J.* **109**, 2562–2573 (2015). doi: 10.1016/j.bpj.2015.11.003; pmid: 26682814
39. T. Mogami, T. Kon, K. Ito, K. Sutoh, Kinetic characterization of tail swing steps in the ATPase cycle of *Dictyostelium* cytoplasmic dynein. *J. Biol. Chem.* **282**, 21639–21644 (2007). doi: 10.1074/jbc.M701914200; pmid: 17548361
40. B. J. Reddy *et al.*, Load-induced enhancement of Dynein force production by LIS1-NudE in vivo and in vitro. *Nat. Commun.* **7**, 12259 (2016). doi: 10.1038/ncomms12259; pmid: 27489054
41. C. Leidel, R. A. Longoria, F. M. Gutierrez, G. T. Shubeita, Measuring molecular motor forces in vivo: Implications for tug-of-war models of bidirectional transport. *Biophys. J.* **103**, 492–500 (2012). doi: 10.1016/j.bpj.2012.06.038; pmid: 22947865
42. M. Wacke, G. Thiel, Electrically triggered all-or-none Ca^{2+}-liberation during action potential in the giant alga *Chara*. *J. Gen. Physiol.* **118**, 11–22 (2001). doi: 10.1085/jgp.118.1.11; pmid: 11429441
43. J. Weiss, Y. Goldman, M. Morad, Electromechanical properties of the single cell-layered heart of tunicate *Boltenia ovifera* (sea potato). *J. Gen. Physiol.* **68**, 503–518 (1976). doi: 10.1085/jgp.68.5.503; pmid: 993769
44. P. Bouchard, S. M. Penningroth, A. Cheung, C. Gagnon, C. W. Bardin, *erythro*-9-[3-(2-Hydroxynonyl)]adenine is an inhibitor of sperm motility that blocks dynein ATPase and protein carboxylmethylase activities. *Proc. Natl. Acad. Sci. U.S.A.* **78**, 1033–1036 (1981). doi: 10.1073/pnas.78.2.1033; pmid: 6453342
45. J. Lin *et al.*, Building blocks of the nexin-dynein regulatory complex in *Chlamydomonas* flagella. *J. Biol. Chem.* **286**, 29175–29191 (2011). doi: 10.1074/jbc.M111.241760; pmid: 21700706
46. D. N. Mastronarde, Automated electron microscope tomography using robust prediction of specimen movements. *J. Struct. Biol.* **152**, 36–51 (2005). doi: 10.1016/j.jsb.2005.07.007; pmid: 16182563
47. J. R. Kremer, D. N. Mastronarde, J. R. McIntosh, Computer visualization of three-dimensional image data using IMOD. *J. Struct. Biol.* **116**, 71–76 (1996). doi: 10.1006/jsbi.1996.0013; pmid: 8742726
48. G. Harauz, M. Van Heel, Exact filters for general geometry three dimensional reconstruction. *Optik (Stuttg.)* **73**, 146–156 (1986).
49. E. F. Pettersen *et al.*, UCSF Chimera—A visualization system for exploratory research and analysis. *J. Comput. Chem.* **25**, 1605–1612 (2004). doi: 10.1002/jcc.20084; pmid: 15264254
50. S. Chifflet, A. Torriglia, R. Chiesa, S. Tolosa, A method for the determination of inorganic phosphate in the presence of labile organic phosphate and high concentrations of protein: Application to lens ATPases. *Anal. Biochem.* **168**, 1–4 (1988). doi: 10.1016/0003-2697(88)90002-4; pmid: 2834977
51. A. J. Roberts, T. Kon, P. J. Knight, K. Sutoh, S. A. Burgess, Functions and mechanics of dynein motor proteins. *Nat. Rev. Mol. Cell Biol.* **14**, 713–726 (2013). doi: 10.1038/nrm3667; pmid: 24064538

ACKNOWLEDGMENTS

We thank D. T. N. Chen and Z. Dogic (Brandeis University) for providing sea urchin sperm, suggestions on ATP reactivation of axonemes, and a light microscopy movie of a swimming sperm cell (Movie 1). We are grateful to C. Xu for providing electron microscopy training and management of the electron microscopy facility at Brandeis University, M. Porter (University of Minnesota) for providing the anti-IC138 antibody, K. Jaqaman (University of Texas Southwestern Medical Center) for experimental suggestions, and the team from XVIVO Scientific Animations for Movie 1. We are also grateful to W. J. Snell, M. Henne, S. Schmid (University of Texas Southwestern Medical Center), M. Porter, and C. Barber for critically reading the manuscript. We also acknowledge P. Satir, I. Gibbons, C. Brokaw, and others in the cilia field for their pioneering studies of ciliary motility. **Funding:** This work was supported by funding from the National Institutes of Health (GM083122 to D.N.) and March of Dimes Foundation (to D.N.). **Author contributions:** D.N. conceived and directed the study. J.L. performed the experiments. J.L. and D.N. analyzed the data and wrote the manuscript. **Competing interests:** The authors declare no competing interests. **Data and materials availability:** All original cryo-ET data of sea urchin sperm flagella have been deposited in the Electron Microscopy Public Image Archive (EMPIAR) under ID codes EMPIAR-10157 and EMPIAR-10158. The 3D averaged structures of all major classes of the ODAs and I1 dynein have been deposited in the Electron Microscopy Data Bank (EMDB) under ID codes EMD-8835, EMD-8836, EMD-8837, and EMD-8838. All other data are available in the manuscript or the supplementary materials.

SUPPLEMENTARY MATERIALS

www.sciencemag.org/content/360/6387/eaar1968/suppl/DC1
Figs. S1 to S5
Tables S1 and S2
References (*52*–*54*)
Movies S1 to S5

13 October 2017; accepted 20 February 2018
10.1126/science.aar1968

Asymmetric distribution and spatial switching of dynein activity generates ciliary motility

Jianfeng Lin and Daniela Nicastro

Science, **360** (6387), eaar1968.
DOI: 10.1126/science.aar1968

Switching how to make flagella beat

Motile cilia and flagella are hairlike cellular appendages that power the movement of individual cells or liquid across tissues, as exemplified by the cilia found in airways. The question of how they move in rhythmic oscillations has puzzled scientists for centuries. Lin and Nicastro used cryo–electron tomography (cryo-ET) to visualize the activity states of individual dynein motors with respect to their locations within beating flagella. They observed an asymmetric distribution of dynein activity and the switching of conformations of dyneins and their regulators between opposite sides of active flagella. The results confirm the switching aspect of the prevailing “switch-point” hypothesis but change the view with respect to how dynein activities are coordinated to drive flagellar motility.

Science, this issue p. eaar1968

Science (ISSN 1095-9203) is published by the American Association for the Advancement of Science. 1200 New York Avenue NW, Washington, DC 20005. The title *Science* is a registered trademark of AAAS.